

Coherent infrared multidimensional spectra of the OH stretching band in liquid water simulated by direct nonlinear exciton propagation

Cyril Falvo, Benoit Palmieri, and Shaul Mukamel^{a)}

Department of Chemistry, University of California, Irvine, California 92697, USA

(Received 28 January 2009; accepted 28 March 2009; published online 8 May 2009)

The two-dimensional vibrational response of the disordered strongly fluctuating OH exciton band in liquid water is investigated using a new simulation protocol. The direct nonlinear exciton propagation generalizes the nonlinear exciton equations to include nonadiabatic time dependent Hamiltonian and transition dipole fluctuations. The excitonic picture is retained and the large cancellation between Liouville pathways is built-in from the outset. The sensitivity of the photon echo and double-quantum-coherence techniques to frequency fluctuations, molecular reorientation, intermolecular coupling, and the two-exciton coherence is investigated. The photon echo is particularly sensitive to the frequency fluctuations and molecular reorientation, whereas the double-quantum coherence provides a unique probe for intermolecular couplings and two-exciton coherence. © 2009 American Institute of Physics. [DOI: [10.1063/1.3120771](https://doi.org/10.1063/1.3120771)]

I. INTRODUCTION

Nonlinear Infrared spectroscopy is a major tool for studying the dynamics of molecules in the condensed phase. Two principal types of theoretical approaches have been developed for simulating and analyzing the nonlinear response of assemblies of identical molecules forming vibrational excitons.^{1,2,36} The sum over states (SOS) provides a convenient low-cost algorithm for computing two-dimensional (2D) signals by recasting them in terms of combinations of correlation functions. Based on the SOS, the cumulant expansion of Gaussian fluctuations method can account for fluctuations of arbitrary time scales and offers a unified description that interpolates between fast (motional narrowing) and slow (inhomogeneous broadening) fluctuations limits. This formalism has several limitations. (1) It only describes Gaussian diagonal fluctuations of the energy. It cannot account for fluctuations of mode couplings and transition dipoles and for non-Gaussian distributions of fluctuations. (2) It uses a fixed exciton basis and neglects fluctuations in the eigenstates. Strong structural fluctuations in proteins and molecular liquids such as water³ or formamide⁴ may not be accounted for. (3) The third order response requires the explicit computation of doubly excited states [$\sim N(N+1)/2$ two exciton states] for N coupled chromophores, followed by a sum over all allowed transitions between the one- and two-exciton manifolds. Practical applications have so far been limited to small peptides ($N < 50$).⁵ (4) Massive cancellations among individual Liouville pathways limit the accuracy and complicate the physical interpretation of signals.^{6–8} The individual contributions to the nonlinear response (Liouville space pathways) scale as $\sim N^2$, whereas the signal (their sum) only scales as $\sim N$. This effect stems from the fact that only when all interactions with the laser fields occur within a coherence size, they contribute to the signal. Excitations at

far away sites that do not communicate with each other make $\sim N^2$ contributions to the individual pathways that eventually cancel out once the pathways are summed over.^{6–8}

The quasiparticle approach which is based on the nonlinear exciton equations (NEEs)^{2,9–11} resolves points (3) and (4), making it most suitable to large proteins and aggregates. This protocol avoids the tedious repeated diagonalization of two-exciton states by introducing an exciton scattering matrix. The cancellations of $\sim N^2$ terms are built-in from the outset and individual pathways are never calculated. However, all applications so far employed a fixed basis and were limited to weak fluctuations with either very fast or very slow timescales.

Limitations (1) and (2) can be resolved by the numerical integration of the Schrödinger equation (NISE).^{12,13} This SOS technique has been applied recently to the nonlinear vibrational response of alanine dipeptide,¹³ liquid *N,N*-dimethyl-formamide,¹⁴ *N*-methyl-acetamide,¹⁵ trpzip2 β -hairpin peptide,¹⁶ and liquid water.³ A much less computationally intensive method, the time-average approximation (TAA), has been introduced by Skinner and Auer¹⁷ and Jansen and Ruszel.¹⁸ By including a free timescale parameter which separates slow from fast fluctuations, the TAA creates an interpolation between uncoupled chromophores with fast fluctuations and the coupled system in the inhomogeneous limit.¹⁷ The NISE and TAA have been compared recently.¹⁸ Note, however, that both are based on the SOS approach and compute individual Liouville pathways so the point (4) is not addressed.

In this paper we develop a direct nonlinear exciton propagation (NEP) method that relaxes all (1)–(4) limitations by extending the NEE to include Hamiltonian fluctuations on an arbitrary timescale. We follow the same derivation of the connection between the SOS and the NEE expression as described in Ref. 19, except that we retain the time dependent Hamiltonian and average over stochastic realizations only at

^{a)}Electronic mail: smukamel@uci.edu.

the end. The NEE equations of motion (rather than the Schrödinger equation) are integrated numerically.

Numerous studies have been dedicated to exploring the structure and dynamics of liquid water which are essential for many physical and biological processes. In particular, nonlinear IR spectroscopy has been widely used on dilute HOD in either H₂O or D₂O (Refs. 20–28) and more recently in neat water.^{3,29–34} The isotope labeling in HOD enables to isolate a single OH (or OD) vibration out of the broad absorption band of the liquid, which acts as a heat bath. The HOD molecule then provides a local probe of the structure and dynamics of the surrounding water. This probe eliminates the intermolecular vibrational couplings which cause a strong excitonic delocalization in neat water, thus simplifying the analysis. Both neat water and HOD were studied in bulk water^{3,20–24,29–31} and in confined environment.^{25–28,32,34} One interesting challenge of nonlinear spectroscopy of water is how to disentangle the influence of orientational dynamics, population relaxation, frequency fluctuations, and wave function delocalization. Using the NEP, we investigate the sensitivity of nonlinear techniques to both the excitonic coupling and the two-exciton coherence in liquid water.

The present work uses the same molecular dynamics (MD) simulation protocol developed in Refs. 3 and 35. The symmetric and asymmetric OH stretching are treated quantum mechanically while the translations and rotations are included classically using MD based on the SPC/E model. The bending vibration is neglected and the OH vibrations are described by a fluctuating adiabatic Hamiltonian. Three types of third order signals can be generated by three pulses with wavevector \mathbf{k}_1 , \mathbf{k}_2 , and \mathbf{k}_3 . These are generated in the direction $\mathbf{k}_1 = -\mathbf{k}_1 + \mathbf{k}_2 + \mathbf{k}_3$ (photon echo), $\mathbf{k}_{II} = \mathbf{k}_1 - \mathbf{k}_2 + \mathbf{k}_3$ and $\mathbf{k}_{III} = \mathbf{k}_1 + \mathbf{k}_2 - \mathbf{k}_3$ (double-quantum coherence). In Refs. 3 and 35, the NISE methodology was used to compute the $\mathbf{k}_1 + \mathbf{k}_{II}$ signal. In this paper, we adopt the same model Hamiltonian and MD trajectory to compute all three signals for two pulse polarization configurations. We investigate the orientational dynamics of water molecules and compare the sensitivity of the three techniques to the intermolecular couplings and the two-exciton coherence.

In Sec. II, we present the formal expressions for the signals. Section III describes the NEP computational algorithm. The simulations are presented in Sec. IV. Conclusions are given in Sec. V.

II. NONLINEAR RESPONSE OF DISORDERED EXCITONS

We consider a system of coupled vibrations described by the effective exciton Hamiltonian,^{2,36}

$$H(t) = \sum_{ij} h_{ij}(t) B_i^\dagger B_j + \sum_{ijkl} U_{ijkl}(t) B_i^\dagger B_j^\dagger B_k B_l, \quad (1)$$

where B_i^\dagger and B_i are, respectively, boson creation and annihilation operator of the i th vibration [$[B_i, B_j^\dagger] = \delta_{ij}$]. h_{ij} is the one-exciton Hamiltonian and U_{ijkl} denotes the exciton-exciton interaction which satisfies $U_{ijkl} = U_{jikl} = U_{ijlk}$. We assume adiabatic decoupling between the high-frequency quantum vibrations (vibrational excitons) which are probed by the spectroscopic experiment and are treated explicitly, and the slow low-frequency classical vibrations which are included implicitly through the fluctuating parameters in the Hamiltonian $H(t)$. The Hamiltonian $H(t)$ conserves the number of excitons $v = \sum_i B_i^\dagger B_i$ and is thus block diagonal. Three blocks are relevant for the present study: the ground state and the one-exciton and two-exciton blocks.

The coupling of the vibrations to the optical field is

$$H_{int}(t) = -\mathbf{E}(\mathbf{r}, t) \cdot \mathbf{V}(t), \quad (2)$$

where

$$\mathbf{V}(t) = \sum_i \boldsymbol{\mu}_i(t) (B_i(t) + B_i^\dagger(t)) \quad (3)$$

is the dipole operator and $\boldsymbol{\mu}_i(t)$ are the transition dipoles.

We shall calculate the third order response function,^{1,36}

$$S_{\nu_4 \nu_3 \nu_2 \nu_1}^{(3)}(\tau_4, \tau_3, \tau_2, \tau_1) = \left(\frac{i}{\hbar} \right)^3 \langle [[[V_{\nu_4}(\tau_4), V_{\nu_3}(\tau_3)], V_{\nu_2}(\tau_2)], V_{\nu_1}(\tau_1)] \rangle, \quad (4)$$

where ν_i are Cartesian polarization indices. Since the water OH stretching frequency is high compared to the temperature $h_{ii} \gg k_B T$, the excitonic system is initially in the ground state $|g\rangle$. The ensemble average $\langle \dots \rangle$ needs to be computed over the quantum states of the operator H as well as the slow classical degrees of freedom by averaging over the stochastic functions $h_{ij}(t)$, $U_{ijkl}(t)$, and $\mu_{i,a}(t)$. The latter can be carried out by integration over the initial time. The average of an operator $A(t; t_0)$ is

$$\langle A(t + t_0; t_0) \rangle = \lim_{T \rightarrow \infty} \frac{1}{2T} \int_{-T}^T dt_0 \langle g | A(t + t_0; t_0) | g \rangle. \quad (5)$$

The three nested commutators in Eq. (4) yield eight Liouville space pathways. Each nonlinear technique selects a subgroup of these pathways.^{1,36} In the following, we present the photon-echo signal generated in the direction $\mathbf{k}_1 = -\mathbf{k}_1 + \mathbf{k}_2 + \mathbf{k}_3$. The other two signals $\mathbf{k}_{II} = \mathbf{k}_1 - \mathbf{k}_2 + \mathbf{k}_3$ and $\mathbf{k}_{III} = \mathbf{k}_1 + \mathbf{k}_2 - \mathbf{k}_3$ (double-quantum coherence) experiments are calculated similarly in Appendices A and B.

Three pathways contribute to the photon-echo signal,^{2,36}

$$S_{\nu_4 \nu_3 \nu_2 \nu_1}^{k_1}(\tau_4, \tau_3, \tau_2, \tau_1) = \left(\frac{i}{\hbar} \right)^3 \sum_{n_1 n_2 n_3 n_4} \mu_{n_1; \nu_1}(\tau_1) \mu_{n_2; \nu_2}(\tau_2) \mu_{n_3; \nu_3}(\tau_3) \mu_{n_4; \nu_4}(\tau_4) \times (\langle g | B_{n_1} \mathcal{U}(\tau_1, \tau_2) B_{n_2}^\dagger \mathcal{U}(\tau_2, \tau_4) B_{n_4} \mathcal{U}(\tau_4, \tau_3) B_{n_3}^\dagger | g \rangle \\ + \langle g | B_{n_1} \mathcal{U}(\tau_1, \tau_3) B_{n_3}^\dagger \mathcal{U}(\tau_3, \tau_4) B_{n_4} \mathcal{U}(\tau_4, \tau_2) B_{n_2}^\dagger | g \rangle - \langle g | B_{n_1} \mathcal{U}(\tau_1, \tau_4) B_{n_4} \mathcal{U}(\tau_4, \tau_3) B_{n_3}^\dagger \mathcal{U}(\tau_3, \tau_2) B_{n_2}^\dagger | g \rangle), \quad (6)$$

where $\mathcal{U}(\tau_2, \tau_1)$ denotes the evolution operator of the vibrations,

$$\mathcal{U}(\tau_2, \tau_1) = \exp_+ \left(-\frac{i}{\hbar} \int_{\tau_1}^{\tau_2} H(\tau) d\tau \right) \quad (7)$$

and \exp_+ is the time ordered exponential. The three terms in Eq. (6) correspond, respectively, to the ground state bleaching (GSB), excited state emission (ESE), and excited state absorption (ESA) contributions. To simplify our notation, in

Eq. (6) we have omitted the integration over the initial time [Eq. (5)]. Equations (6) can be simplified by introducing the one-exciton and two-exciton Green's functions

$$G_{n_2, n_1}(\tau_2, \tau_1) = \langle g | B_{n_2} \mathcal{U}(\tau_2, \tau_1) B_{n_1}^\dagger | g \rangle, \quad (8)$$

$$G_{n_2 m_2, n_1 m_1}(\tau_2, \tau_1) = \langle g | B_{n_2} B_{m_2} \mathcal{U}(\tau_2, \tau_1) B_{n_1}^\dagger B_{m_1}^\dagger | g \rangle. \quad (9)$$

Substituting Eqs. (8) and (9) in Eq. (6) gives

$$\begin{aligned} S_{\nu_4 \nu_3 \nu_2 \nu_1}^{k_1}(\tau_4, \tau_3, \tau_2, \tau_1) = & \left(\frac{i}{\hbar} \right)^3 \sum_{n_1 n_2 n_3 n_4} \mu_{n_1; \nu_1}(\tau_1) \mu_{n_2; \nu_2}(\tau_2) \mu_{n_3; \nu_3}(\tau_3) \mu_{n_4; \nu_4}(\tau_4) \times \\ & \left(G_{n_4, n_3}(\tau_4, \tau_3) G_{n_2, n_1}^*(\tau_2, \tau_1) \right. \\ & \left. + G_{n_4, n_2}(\tau_4, \tau_2) G_{n_3, n_1}^*(\tau_3, \tau_1) - \sum_{m_1 m_2} G_{n_4 m_1, n_3 m_2}(\tau_4, \tau_3) G_{m_2, n_2}(\tau_3, \tau_2) G_{m_1, n_1}^*(\tau_4, \tau_1) \right). \end{aligned} \quad (10)$$

For harmonic vibrations ($U_{ijk}(t)=0$) the two-exciton Green's function is given by

$$\begin{aligned} \mathcal{G}_{n_2 m_2, n_1 m_1}^{(0)}(\tau_2, \tau_1) = & G_{n_2 n_1}(\tau_2, \tau_1) G_{m_2 m_1}(\tau_2, \tau_1) \\ & + G_{n_2 m_1}(\tau_2, \tau_1) G_{n_1 m_2}(\tau_2, \tau_1). \end{aligned} \quad (11)$$

Substituting Eq. (11) in Eq. (10) and using the relation

$$G_{ij}(\tau_i, \tau_j) = \sum_k G_{ik}(\tau_i, \tau_k) G_{kj}(\tau_k, \tau_j), \quad (12)$$

we find that the k_1 response function [Eq. (10)] vanishes. This is to be expected since the harmonic system is linear

and all nonlinear response functions must vanish. To exploit this cancellation, we introduce the Bethe-Salpeter equation (two particle Dyson equation),³⁷

$$\begin{aligned} & G_{n_2 m_2, n_1 m_1}(\tau_2, \tau_1) \\ & = \mathcal{G}_{n_2 m_2, n_1 m_1}^{(0)}(\tau_2, \tau_1) - \frac{i}{\hbar} \sum_{n_3 m_3 n_4 m_4} \int_{\tau_1}^{\tau_2} ds \mathcal{G}_{n_2 m_2, n_4 m_4}^{(0)}(\tau_2, s) \\ & \times U_{n_4 m_4 n_3 m_3}(s) \mathcal{G}_{n_3 m_3, n_1 m_1}(s, \tau_1). \end{aligned} \quad (13)$$

Substituting Eq. (13) in Eq. (10) we finally get

$$\begin{aligned} S_{\nu_4 \nu_3 \nu_2 \nu_1}^{k_1}(\tau_4, \tau_3, \tau_2, \tau_1) = & 2 \left(\frac{i}{\hbar} \right)^4 \sum_{n_1 n_2 n_3 n_4} \sum_{m_1 m_2 m_3 m_4 p_2} \mu_{n_1; \nu_1}(\tau_1) \mu_{n_2; \nu_2}(\tau_2) \mu_{n_3; \nu_3}(\tau_3) \mu_{n_4; \nu_4}(\tau_4) \\ & \times \int_{\tau_3}^{\tau_4} ds G_{n_4, m_4}(\tau_4, s) U_{m_4 m_1 m_3 m_2}(s) \mathcal{G}_{m_3 m_2, n_3 p_2}(s, \tau_3) G_{p_2, n_2}(\tau_3, \tau_2) G_{m_1, n_1}^*(s, \tau_1). \end{aligned} \quad (14)$$

The nonlinear response is now given by a time integral over the interval s between interactions with the k_3 and k_4 pulses. Note that the exact cancellation of the harmonic part in Eq. (6) has been accounted for, and Eq. (14) now explicitly depends on the anharmonicity U_{ijkl} to first order [higher orders enter through $\mathcal{G}(s, \tau_3)$]. Alternatively, Eq. (14) can be derived using the NEE approach. This derivation is detailed in Appendix C. Equation (14) can be represented by the single Feynman diagram shown in Fig. 1(a). In this diagram, time evolves from bottom to top. A wavy line represents an interaction with the laser field. A solid line represents a one-

exciton Green's function propagating forward (upward arrow) or backward (downward arrow). A double line represents the two-exciton Green's function \mathcal{G} . Finally the gray band represents the region between times τ_3 and τ_4 where exciton scattering takes place. This scattering stems from the interaction U_{ijkl} which splits the two-exciton Green's function into an exciton propagating forward from s to τ_4 and a second exciton propagating backward from s to τ_1 . Similar expressions for the k_{II} and k_{III} techniques are given in Appendices A and B, respectively, and represented by Figs. 1(b) and 1(c).

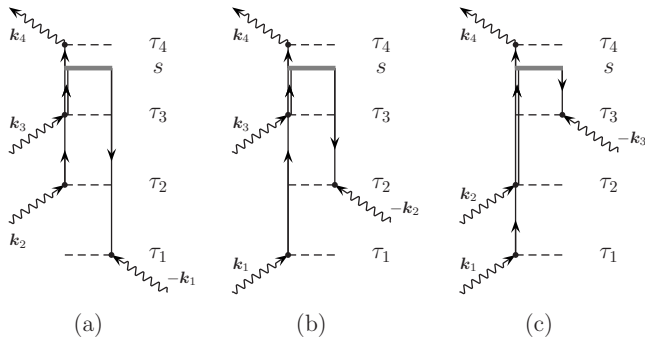


FIG. 1. Feynman diagrams representing various third order signals in the quasi particle representation (Ref. 2) (a) k_I [Eq. (14)], (b) k_{II} [Eq. (A2)], and (c) k_{III} [Eq. (B2)].

III. THE NEP ALGORITHM

For computational efficiency, we do not calculate Green's function in Eq. (14) but we compute the time dependent one- and two-exciton wave functions,

$$\psi_{m_1; \nu_1}^{(1)}(s; \tau_1) = \sum_{n_1} G_{m_1, n_1}(s, \tau_1) \mu_{n_1; \nu_1}(\tau_1), \quad (15)$$

$$\begin{aligned} \psi_{m_1 m_2; \nu_1; \nu_2}^{(2)}(s; \tau_2; \tau_1) \\ = \sum_{n_2 n_1} \mathcal{G}_{m_2 m_1, n_2 n_1}(s, \tau_2) \mu_{n_2; \nu_2}(\tau_2) \psi_{m_1; \nu_1}^{(1)}(\tau_2; \tau_1), \end{aligned} \quad (16)$$

where $\psi_{m_1; \nu_1}^{(1)}(s; \tau_1)$ describe the propagation of a single exciton created at time τ_1 by the action of the transition dipole $\mu_{n_1; \nu_1}(\tau_1)$, while $\psi_{m_1 m_2; \nu_1}^{(2)}(s; \tau_2; \tau_1)$ describe the two-exciton propagation. The first exciton is created at time τ_1 and propagates until time τ_2 where a second exciton is created and propagate until time s . At the initial time $s=\tau_2$, the two-exciton wave function is given by a symmetrized product of the one-exciton wave function $\psi_{m_1; \nu_1}^{(1)}(\tau_2; \tau_1)$ and the transition dipole $\mu_{m_2; \nu_2}(\tau_2)$,

$$\begin{aligned} \psi_{m_1 m_2; \nu_1; \nu_2}^{(2)}(\tau_2; \tau_2; \tau_1) \\ = \psi_{m_1; \nu_1}^{(1)}(\tau_2; \tau_1) \mu_{m_2; \nu_2}(\tau_2) + \psi_{m_2; \nu_2}^{(1)}(\tau_2; \tau_1) \mu_{m_1; \nu_1}(\tau_2). \end{aligned} \quad (17)$$

Using these definitions, we can recast Eq. (14) in the form

$$\begin{aligned} S_{\nu_4 \nu_3 \nu_2 \nu_1}^{k_I}(\tau_4, \tau_3, \tau_2, \tau_1) \\ = 2 \left(\frac{i}{\hbar} \right)^4 \sum_{n_4} \mu_{n_4; \nu_4}(\tau_4) R_{n_4; \nu_3 \nu_2 \nu_1}^{k_I}(\tau_4, \tau_3, \tau_2, \tau_1), \end{aligned} \quad (18)$$

with

$$\begin{aligned} R_{n_4; \nu_3 \nu_2 \nu_1}^{k_I}(\tau_4, \tau_3, \tau_2, \tau_1) \\ = \sum_{m_4} \int_{\tau_3}^{\tau_4} ds G_{n_4, m_4}(\tau_4, s) X_{m_4; \nu_3 \nu_2 \nu_1}^{k_I}(s; \tau_3, \tau_2, \tau_1) \end{aligned} \quad (19)$$

and

$$\begin{aligned} X_{m_4; \nu_3 \nu_2 \nu_1}^{k_I}(s; \tau_3, \tau_2, \tau_1) \\ = \sum_{m_1 m_2 m_3} U_{m_4 m_1 m_3 m_2}(s) \\ \times \psi_{m_3 m_2; \nu_3; \nu_2}^{(2)}(s; \tau_3; \tau_2) \psi_{m_1; \nu_1}^{(1)*}(s; \tau_1). \end{aligned} \quad (20)$$

The one- and two-exciton wave functions are computed by direct integration of the Schrödinger equation. For the one-exciton wave function we have

$$i\hbar \frac{\partial}{\partial t} |\psi_{\nu_1}^{(1)}(t; \tau_1)\rangle = H(t) |\psi_{\nu_1}^{(1)}(t; \tau_1)\rangle, \quad (21)$$

where $|\psi_{\nu}^{(1)}(t; t_0)\rangle = \sum_n \psi_{n; \nu}^{(1)}(t; t_0) B_n^\dagger |g\rangle$. A similar equation holds for the two-exciton wave function,

$$i\hbar \frac{\partial}{\partial t} |\psi_{\nu_1}^{(2)}(t; \tau_2; \tau_1)\rangle = H(t) |\psi_{\nu_1}^{(2)}(t; \tau_2; \tau_1)\rangle, \quad (22)$$

where $|\psi_{\nu_1 \nu_2}^{(2)}(t; \tau_2; \tau_1)\rangle = \frac{1}{2} \sum_{n_1 n_2} \psi_{n_1 n_2; \nu_1; \nu_2}^{(2)}(t; \tau_2; \tau_1) B_{n_1}^\dagger B_{n_2}^\dagger |g\rangle$.

The response function $S(t_3, t_2, t_1)$ is computed versus the different time intervals between the pulses $t_1 = \tau_2 - \tau_1$, $t_2 = \tau_3 - \tau_2$, and $t_3 = \tau_4 - \tau_3$. Details of our integration procedure used to generate the response function are given in Appendix D. Starting from a fluctuating Hamiltonian trajectory, our simulation protocol for a k_I signal is summarized as follows.

- (1) We choose an initial time τ_1 along the Hamiltonian trajectory.
- (2) The first one-exciton wave function is created at time τ_1 [Eq. (15)] and propagated until time $\tau_1 + t_1 + t_2 + t_3$ using Eq. (D4).
- (3) A second one-exciton wave function is created at time $\tau_1 + t_1$ and propagated until time $\tau_1 + t_1 + t_2$ using Eq. (D4).
- (4) At time $\tau_1 + t_1 + t_2$ the second exciton is used to create a two-exciton wave function [Eq. (17)] which is propagated until time $\tau_1 + t_1 + t_2 + t_3$ using Eq. (D5).
- (5) Using Eqs. (D7) and (20), the function $R_{n_4; \nu_3 \nu_2 \nu_1}(s, \tau_1 + t_1 + t_2, \tau_1 + t_1, \tau_1)$ is computed between $s = \tau_1 + t_1 + t_2$, where $R_{n_4; \nu_3 \nu_2 \nu_1}$ is set to zero and the time $s = \tau_1 + t_1 + t_2 + t_3$. The response function is finally given by Eq. (18).

To perform the ensemble averaging, this protocol is repeated over several initial conditions and orientations. A similar protocol may be used for the other two experiments (k_{II} and k_{III}), where the single and two-exciton wave functions are created at different times, as given by Eqs. (A3) and (B3).

IV. THE OH STRETCH OF LIQUID WATER

A. The vibrational exciton Hamiltonian

We used the following effective Hamiltonian for M water molecules each having two OH stretching modes (symmetric and asymmetric):

$$\begin{aligned}
H(t) = & \hbar \sum_{i=1}^M \sum_{\alpha=a,s} \omega_{i\alpha}(t) B_{i\alpha}^\dagger B_{i\alpha} \\
& + \hbar \sum_{i,j=1}^M \sum_{\alpha,\beta=a,s} J_{i\alpha,j\beta}(t) B_{i\alpha}^\dagger B_{j\beta} \\
& - \frac{\hbar}{2} \sum_{i=1}^M \sum_{\alpha,\beta=a,s} \Delta_{i\alpha,i\beta}(t) B_{i\alpha}^\dagger B_{i\beta}^\dagger B_{i\alpha} B_{i\beta}, \quad (23)
\end{aligned}$$

where $\omega_{i\alpha}(t)$ is the harmonic frequency of the mode α (symmetric or asymmetric) of molecule i at time t . $\Delta_{i\alpha,i\beta}(t)$ is the intramolecular anharmonicities of molecule i . Intermolecular anharmonicities were neglected. The transition dipole coupling model was used for $J_{i\alpha,j\beta}(t)$ with the dielectric constant $\epsilon=22.1$ chosen to reproduce polarization anisotropy measurement,³⁵

$$\begin{aligned}
J_{i\alpha,j\beta}(t) = & \frac{1 - \delta_{ij}}{4\pi\epsilon R_{ij}^3(t)} [3(\boldsymbol{\mu}_{i\alpha}(t)\mathbf{n}_{ij}(t))(\boldsymbol{\mu}_{j\beta}(t)\mathbf{n}_{ij}(t)) \\
& - \boldsymbol{\mu}_{i\alpha}(t)\boldsymbol{\mu}_{j\beta}(t)]. \quad (24)
\end{aligned}$$

We have used the same Hamiltonian trajectory reported recently.^{3,35} It was obtained by a MD simulation of 64 water molecules at 300 K using periodic boundary conditions and the SPC/E water model. An electrostatic map based on *ab initio* calculations at the MP2/6-31+G(*d,p*) level was used to describe the variation in the Hamiltonian parameters with the electrostatic environment.^{3,35,38} Overall the simulation has $N=2M=128$ vibrational modes. The electrostatic map gives the local Hamiltonian of each water molecule (frequencies, anharmonicities, and transition dipoles) as a function of time.

The quartic anharmonicity in Eq. (23) is diagonal and corresponds to $U_{ijkl}=\Delta_{ij}\delta_{ik}\delta_{jl}/2$ in Eq. (1). This greatly simplifies the numerical protocol. Since, in general, the anharmonic term contains four indices, the calculation of the vector $X_{m_4;\nu_3\nu_2\nu_1}^{k_1}$ [Eq. (20)] takes a time proportional to N^4 . Similarly, propagating the two-exciton state involves the multiplication of the wave function by the operator ΔH [Eq. (D5)], and the corresponding computational time scales as $\sim N^4$. For diagonal anharmonicity the number of indices of U_{ijij} is reduced to 2 and the calculation time of the vector $X_{m_4;\nu_3\nu_2\nu_1}^{k_1}$ becomes $\sim N^2$. In a similar fashion, the operator ΔH contains only harmonic couplings and the multiplication of the wave function of size N^2 by ΔH takes a time $\sim N^3$. Using this approach we have greatly reduced the computational time required for calculation of the nonlinear signals compared with similar computational methods. For example, computation of $S^{k_1}(t_1, 0, t_3)$ for a single trajectory and for the time interval $0 \leq t_1 < 200$ fs and $0 \leq t_3 < 200$ fs using the NEP method requires less than 2 min on a single AMD Athlon® class processor.

B. Results

1. The k_1 and k_{II} signals

Our calculation is based on 50, 1 ps long, Hamiltonian trajectories. Each signal is averaged over 20 random orientations. To remove finite sampling noise, we have filtered the

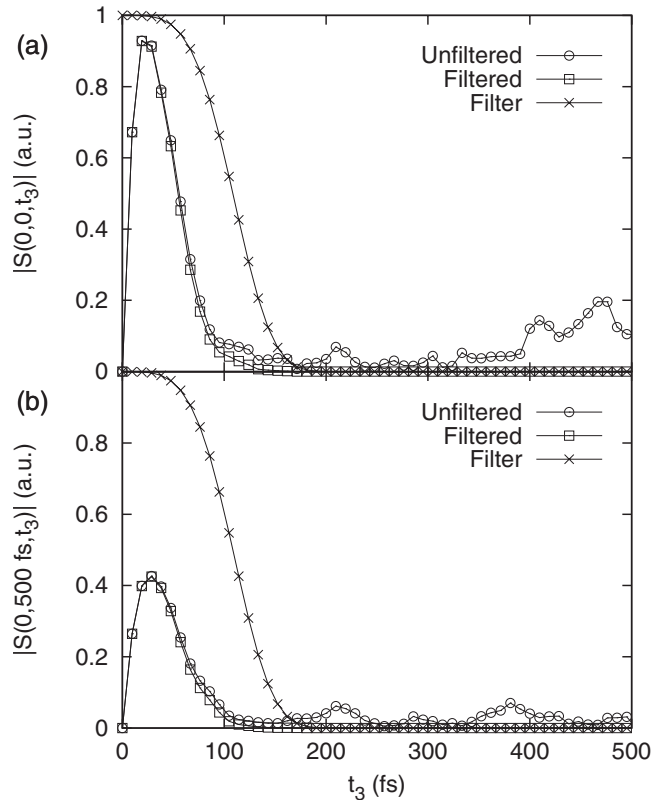


FIG. 2. Computed bare (○) and filtered (□) k_1 signals for $t_1=0$ and $t_2=0$ (a) and $t_2=500$ fs (b) as a function of t_3 . The filter function $F^{k_1,k_1}(0,t_3)$ [Eq. (25)] is also reported (×).

time-domain signals in a similar fashion as done previously^{14,35} by multiplying by the filter function,

$$F^{k_1,k_1}(t_1, t_3) = \exp\left(-\frac{1}{2}\left(\frac{t_1}{T_f}\right)^4 - \frac{1}{2}\left(\frac{t_3}{T_f}\right)^4\right), \quad (25)$$

where $T_f=100$ fs is a cutoff time. Figure 2 compares the bare and filtered k_1 signal for $t_1=0$ and $t_2=0$ [Fig. 2(a)] and $t_2=500$ fs [Fig. 2(b)] versus t_3 . Fig. 2 also reports the filter $F^{k_1,k_1}(0,t_3)$. Note that for $t_1=t_2=0$, all techniques coincide $S^{k_1}(0,0,t_3)=S^{k_{II}}(0,0,t_3)=S^{k_{III}}(0,0,t_3)$. For $t_2=0$, the bare signal increases rapidly in the early times, has its maximum around $t_3 \sim 20$ fs, and then decreases quickly due to the fast vibrational dephasing. For $t_2=500$ fs, the bare signal has its maximum around $t_3 \sim 30$ fs and the decrease is slightly slower than for $t_2=0$. It is clear that amplitude present after $t_3=150$ fs corresponds to noise and should be eliminated from our calculation. As shown in Fig. 2, using the filter $F^{k_1,k_1}(t_1, t_3)$ with a 100 fs cutoff does not modify strongly the signal for both $t_2=0$ and $t_2=500$ fs.

The k_1 and k_{II} signals are represented in the frequency domain as

$$\begin{aligned}
S_{\nu_4\nu_3\nu_2\nu_1}^{k_1 k_{II}}(\Omega_1, \Omega_2, \Omega_3) = & \int_0^\infty \int_0^\infty S_{\nu_4\nu_3\nu_2\nu_1}^{k_1 k_{II}}(t_1, t_2, t_3) \\
& \times e^{i\Omega_1 t_1 + i\Omega_2 t_2 + i\Omega_3 t_3} dt_1 dt_3. \quad (26)
\end{aligned}$$

In order to characterize our simulated 2D-IR spectra, we introduce the diagonal $\gamma_{||}$ and antidiagonal γ_{\perp} widths of the spectra defined as the half-maximum contour line in the ab-

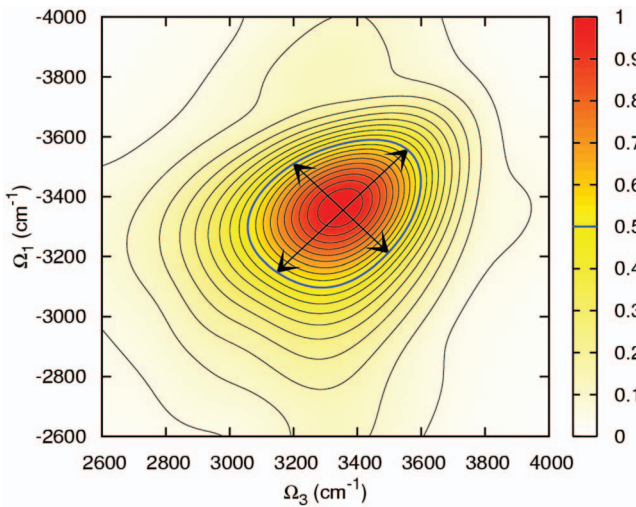


FIG. 3. (Color) The diagonal γ_{\parallel} and antidiagonal γ_{\perp} linewidths for the absolute value of a k_I signal. The blue contour line marks the half-maximum contour.

solute value 2D spectrum as shown on Fig. 3. The k_I signal for the XXXX polarization (all laser pulse with the same polarization) is displayed on Fig. 4 for several time delays $t_2 = 0, 100, 200$, and 500 fs. Two peaks are observed in the imaginary part of the k_I signal. The positive peak comes from the GSB and ESE, while the negative peak from the ESA. The diagonal width, the antidiagonal width, and their ratio are given on Table I. A strong correlation is observed for $t_2=0$ between the excitation frequency (Ω_1) and the probe frequency (Ω_3) as shown by elliptical shape of the absolute value of the signal. The diagonal (antidiagonal) width is 577 cm $^{-1}$ (420 cm $^{-1}$). As t_2 is increased, the ratio $\gamma_{\perp}/\gamma_{\parallel}$ tends toward unity, reflecting loss of correlation. At $t_2=500$ fs, the signal has a circular shape ($\gamma_{\perp}/\gamma_{\parallel} \approx 1$).

It is a common practice to display instead of the photon-echo signal defined as Eq. (26) a signal where the t_1 time

TABLE I. Diagonal width and antidiagonal width of the k_I signal with XXXX polarization (Fig. 4).

t_2 (fs)	γ_{\parallel} (cm $^{-1}$)	γ_{\perp} (cm $^{-1}$)	$\gamma_{\perp}/\gamma_{\parallel}$
0	577	420	0.73
100	560	465	0.83
200	597	502	0.84
500	578	581	1.00

integral is extended to the interval $]-\infty, +\infty[$.³ In our notation we maintain time ordering k_I comes first followed by k_2 and k_3 , and we keep all time intervals positive, a signal with a negative time correspond to a permutation of the two first lasers which is precisely the k_{II} signal. This contribution is often called nonrephasing signal, as opposed to the rephasing signal (photon echo). We define the total signal rephasing plus nonrephasing as the sum of k_I and k_{II} ,

$$S_{\nu_4\nu_3\nu_2\nu_1}^{k_I+k_{II}}(\Omega_1, t_2, \Omega_3) = S_{\nu_4\nu_3\nu_2\nu_1}^{k_I}(-\Omega_1, t_2, \Omega_3) + S_{\nu_4\nu_3\nu_2\nu_1}^{k_{II}}(\Omega_1, t_2, \Omega_3). \quad (27)$$

By integrating over the Ω_1 frequency, this signal corresponds to the impulsive pump-probe signal,

$$S_{\mu\nu}^{PP}(\tau, \omega) = \int d\Omega_1 S_{\mu\nu\nu\nu}^{k_I+k_{II}}(\Omega_1, \tau, \omega), \quad (28)$$

where ω is the dispersed frequency and τ is the time delay between the two pulses with polarizations μ and ν . The k_I , k_{II} , and k_I+k_{II} signals are displayed for $t_2=0$ and $t_2=500$ fs in Fig. 5; each spectrum is normalized to its maximum. The relative maximum with respect to k_I signal at time $t_2=0$ is given in parenthesis. For k_I+k_{II} , the exact same calculation has been conducted recently using the NISE

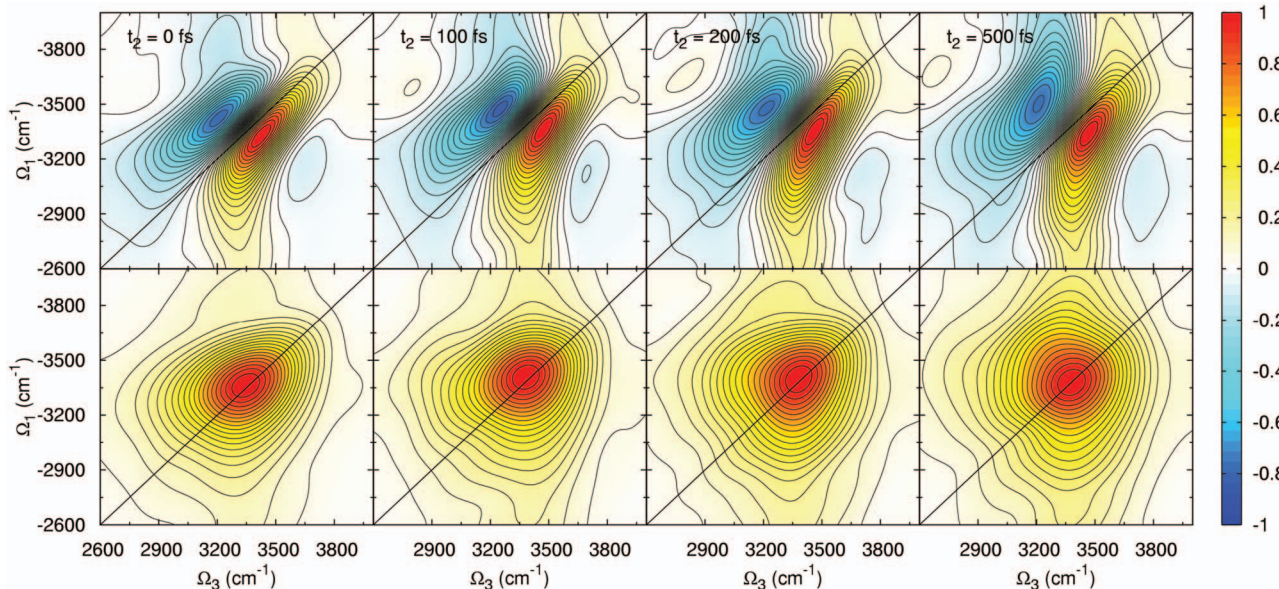


FIG. 4. (Color) k_I XXXX signal for various t_2 delay times. Upper row: imaginary part; lower row: absolute value. Each spectrum is normalized respectively to its maximum.

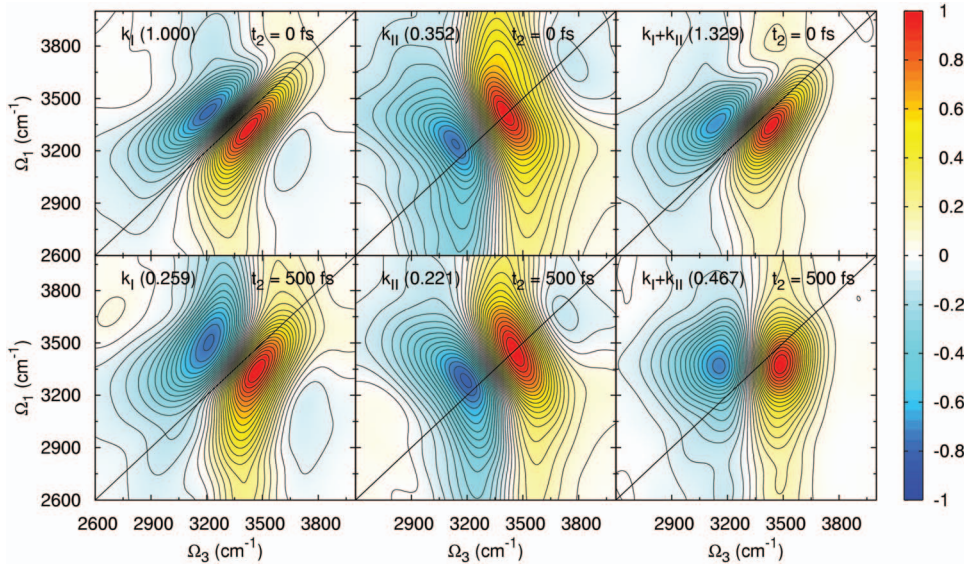


FIG. 5. (Color) k_I , k_{II} , and k_I+k_{II} imaginary part signals with XXXX polarization for $t_2=0$ (upper row) and $t_2=500$ fs (lower row). Each panel is normalized to its maximum. The relative maximum with respect to k_I signal at time $t_2=0$ is indicated in parenthesis. The k_I signal is displayed for negative Ω_1 frequencies.

methodology.^{3,35} Our result gives identical spectra within numerical accuracy.

k_{II} appears very different from k_I , in particular, the two peaks are elongated along the antidiagonal and the signal is broader. This is due to the elimination of the inhomogeneous broadening by the photon echo. The k_{II} signal maximum is only 0.352 compared to that of the photon echo, and consequently the k_I+k_{II} signal is dominated by k_I . The photon-echo signal varies strongly with t_2 . At 500 fs, the maximum decreases to 0.259 of its original value. In contrast, the k_{II} signal shape is hardly affected and its maximum decreases only to 0.221 after 500 fs starting from 0.352 at $t_2=0$. At $t_2=500$ fs, both k_I and k_{II} signals contribute almost equally to the k_I+k_{II} signal. The loss of correlations observed in the photon echo can also be seen in the k_I+k_{II} signal. At $t_2=0$ it is elongated along the diagonal, while at $t_2=500$ fs, it is oriented vertically. This trend has been observed previously.^{3,33,39}

We next consider the k_I and k_{II} signals using the XXYY polarization configuration (k_I and k_2 have parallel polarizations which is perpendicular to that of k_3 and k_4). When the transition dipole magnitude and orientation are fixed, intermolecular couplings neglected and the fluctuations are slow, we expect $S_{XXYY}=S_{XXXX}/3$. However, in our simulations, none of these conditions are true and this relation does not hold. In Fig. 6(a) we display the XXXX and XXYY signals at $t_2=0$ for both k_I and k_{II} . For k_I , the XXXX and XXYY signals are very similar in shape but their relative intensity is not the same. We define the ratio

$$\alpha = \frac{\max|S_{XXXX}|}{\max|S_{XXYY}|}. \quad (29)$$

At $t_2=0$, we found $\alpha=2.72$ for k_I . Deviation from $\alpha=3.0$ is caused by the dynamics of the water molecules and the delocalization of the exciton wave function during t_1 and t_3 .

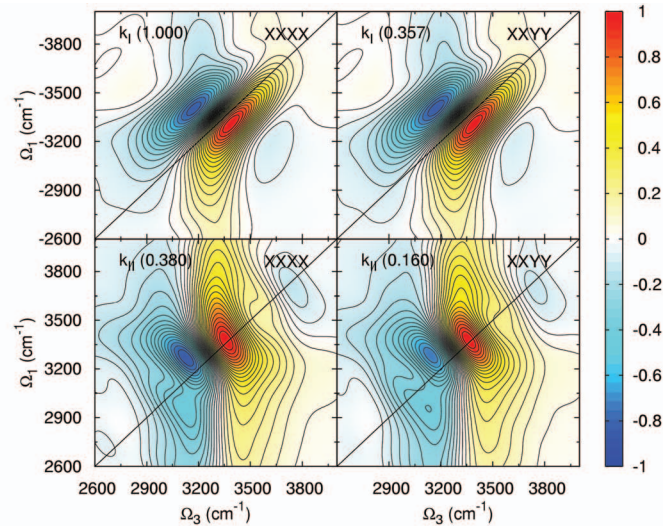
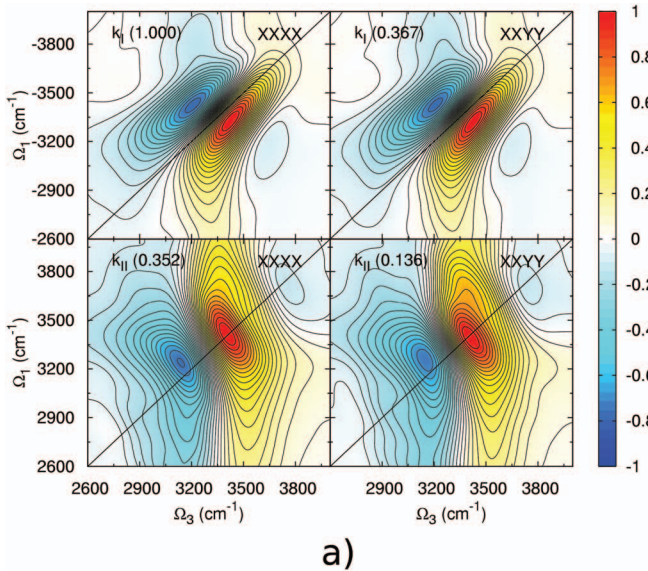


FIG. 6. (Color) k_I and k_{II} signals with polarization XXXX and XXYY for $t_2=0$ for coupled molecules (a) and uncoupled molecules (b). Each panel is normalized to its maximum. The relative maximum with respect to k_I signal at time $t_2=0$ is indicated in parenthesis.

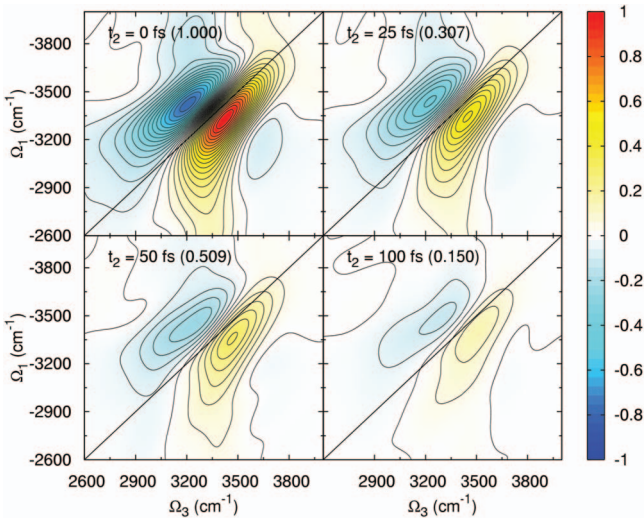


FIG. 7. (Color) k_1 polarization anisotropy signal $S_{XXXX}^{k_1} - S_{XXYY}^{k_1}$ for time $t_2 = 0, 25, 50$, and 100 fs. Each panel is normalized to the maximum of the $t_2 = 0$ signal.

For k_{II} , the shape of the $XXXX$ and $XXYY$ signals are similar but some small differences can be found. In particular, stronger absorption is visible in the range $\Omega_1 = 3500\text{--}3800\text{ cm}^{-1}$ of the positive peak of the $XXYY$ signal. We found $\alpha = 2.43$ for k_{II} . As t_2 is increased, α rapidly decreases toward unity reflecting the loss of correlation between the X and Y directions due to the orientational dynamics of water molecules, the intermolecular coupling, and the vibrational dephasing. To show this effect, we have computed the generalization for the photon echo of the polarization anisotropy commonly used in pump-probe spectroscopy. The difference $S_{XXXX}^{k_1} - S_{XXYY}^{k_1}$ is displayed in Fig. 7 for various t_2 . The k_1 polarization anisotropy signal rapidly vanishes. At $t_2 = 100$ fs, the maximum of the anisotropy signal is only 15% of the $t_2 = 0$ value. The decay of the polarization anisotropy is certainly complex, however, it can be understood as a direct signature

of the fast vibrational dynamics created by the hydrogen bond network.

To explore the sensitivity of the k_1 and k_{II} signals to the intermolecular coupling, we have repeated in Fig. 6(b) the calculations of Fig. 6(a) by setting the coupling $J_{ia,\beta\beta} = 0$. For k_{II} the small difference between $XXXX$ and $XXYY$ signals disappears totally when the molecules are uncoupled, indicating that this difference was clearly due to the intermolecular coupling. For k_1 no difference is apparent in shape but the spectra have different intensities. At $t_2 = 0$ we find $\alpha = 2.79$ for k_1 and $\alpha = 2.57$ for k_{II} . By neglecting the coupling we have made the exciton wave function localized. Only the molecular reorientation and the dephasing now influence the ratio α and its value is now closer to 3. It has been found previously³ that for fixed t_2 the $k_1 + k_{II}$ signal in water is not very sensitive to the intermolecular coupling. Our simulations show that this holds also for k_1 and that k_{II} is slightly more sensitive. However, when varying t_2 the influence of the excitonic coupling appears. Indeed, it is known that the excitonic coupling induces a faster decay of the polarization anisotropy.^{3,40,41}

To investigate the sensitivity of the k_1 and k_{II} signals to the two-exciton coherence, we have computed them also in the mean field approximation.² This neglects the two-exciton coherence by replacing the two-exciton wave function [Eq. (16)] into Eq. (14) by a symmetrized product of two single exciton wave function,

$$\begin{aligned} \psi_{n_1 n_2; \nu_1; \nu_2}^{(2)}(s; \tau_2; \tau_1) &\approx \psi_{n_2; \nu_2}^{(1)}(s; \tau_2) \psi_{n_1; \nu_1}^{(1)}(s; \tau_1) \\ &+ \psi_{n_1; \nu_2}^{(1)}(s; \tau_2) \psi_{n_2; \nu_1}^{(1)}(s; \tau_1). \end{aligned} \quad (30)$$

This approximation greatly reduces the simulation time. The calculation time necessary to compute the two-exciton propagation scales as N^2 instead of N^3 . For our system, computational time was divided by 4 when this approximation is used. Figure 8 shows that the k_1 and k_{II} signals at time t_2

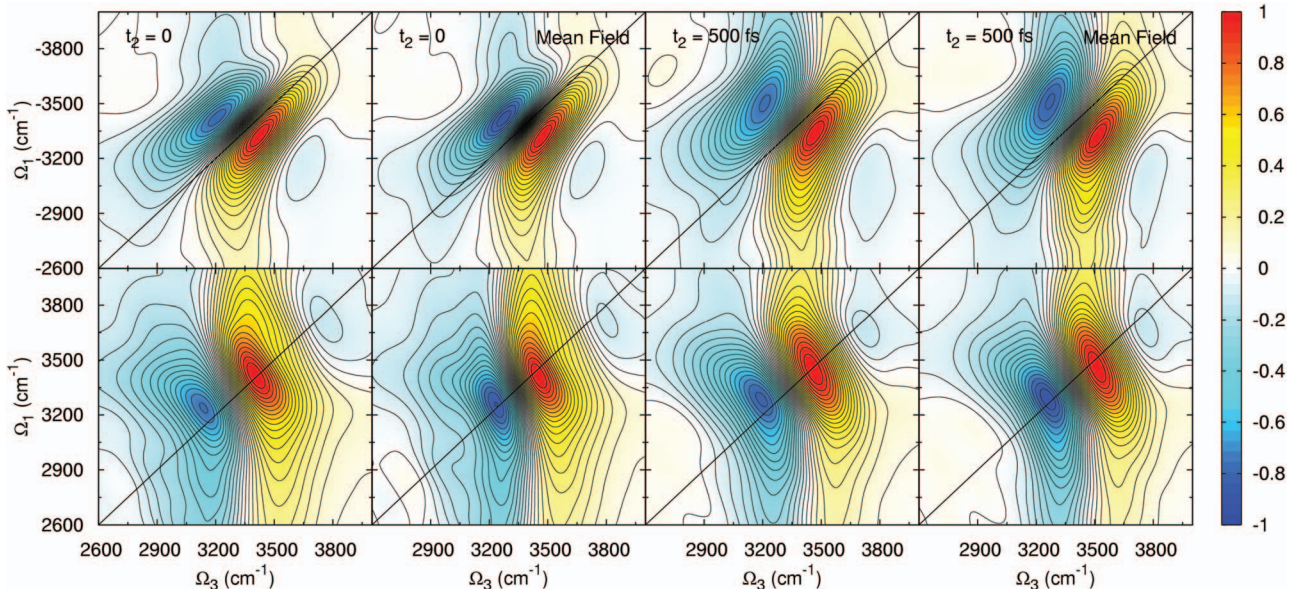


FIG. 8. (Color) Upper row: k_1 signal for $t_2 = 0$ and $t_2 = 500$ fs and the corresponding mean field approximate signals. Lower row: same for the k_{II} signal.

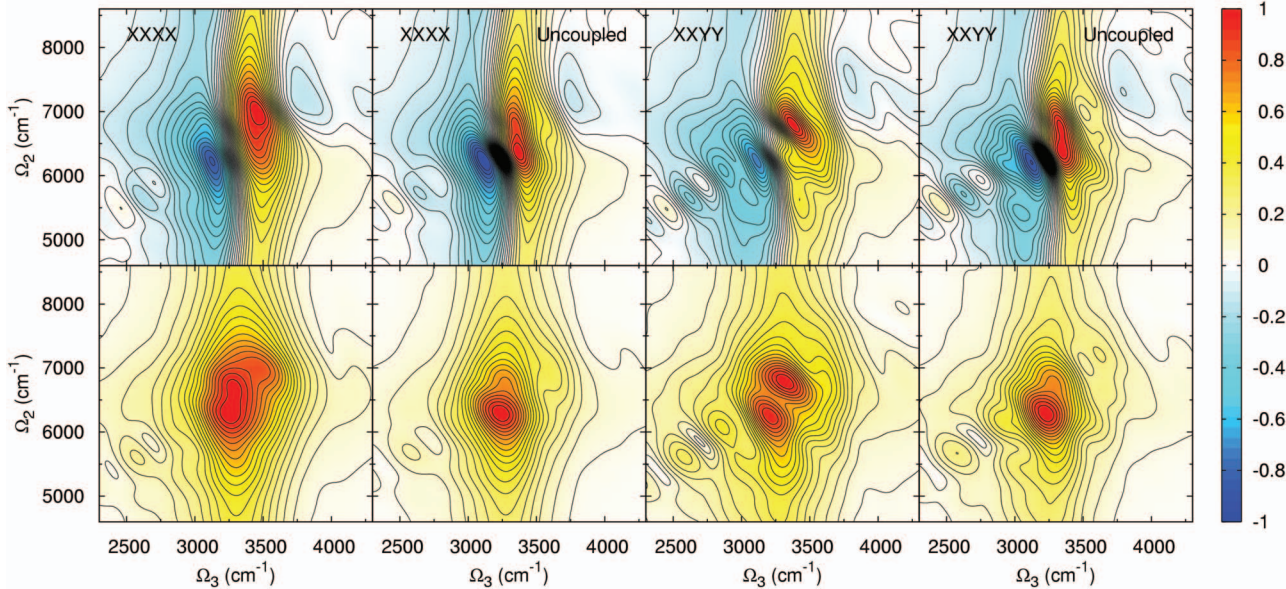


FIG. 9. (Color) XXXX and XXYY k_{III} signal for $t_1=0$ with the corresponding uncoupled signals. Upper row: imaginary part; lower row: absolute value. Each spectrum is normalized to its maximum.

$=0$ and $t_2=500$ fs are very similar to the corresponding mean field spectra.

2. Double-quantum-coherence signals

When varying t_2 , \mathbf{k}_1 and \mathbf{k}_{II} techniques show the fast vibrational dynamics. However, the above simulations demonstrate that for fixed t_2 , \mathbf{k}_1 and \mathbf{k}_{II} techniques are not very sensitive to the intermolecular coupling and the two-exciton coherence. The double-quantum-coherence \mathbf{k}_{III} technique is expected to be more sensitive to latter effects, since it provides a clean projection of two-exciton states.^{2,42} The \mathbf{k}_{III} signals are represented in the frequency domain as

$$S_{\nu_4 \nu_3 \nu_2 \nu_1}^{k_{\text{III}}}(t_1, \Omega_2, \Omega_3) = \int_0^\infty \int_0^\infty S_{\nu_4 \nu_3 \nu_2 \nu_1}^{k_{\text{III}}}(t_1, t_2, t_3) e^{i\Omega_2 t_2 + i\Omega_3 t_3} dt_2 dt_3. \quad (31)$$

In the following simulations, we display the \mathbf{k}_{III} signal in time domain using the following filter:

$$F^{k_{\text{III}}}(t_1, t_3) = \exp\left(-\frac{1}{2}\left(\frac{2t_2}{T_f}\right)^4 - \frac{1}{2}\left(\frac{t_3}{T_f}\right)^4\right). \quad (32)$$

We use the same cutoff $T_f=100$ fs as in the \mathbf{k}_1 and \mathbf{k}_{II} signals. Figure 9 compares the XXXX and XXYY k_{III} signals at $t_1=0$ with and without intermolecular coupling $J_{i\alpha,j\beta}$. The imaginary part shows a negative peak and a positive peak. Intermolecular coupling spreads the signal along the Ω_2 axis which is a direct projection of the two-exciton states. The absolute value spectrum is much stronger with the coupling in the blue side, 6500–7000 cm⁻¹ frequency range. To trace the origin of this effect, we have computed the two-exciton density of states (DOS),

$$\rho(\omega) = \sum_{\lambda} \langle \delta(\omega - \omega_{\lambda}) \rangle, \quad (33)$$

where ω_{λ} are the two-exciton eigenfrequencies. For uncoupled molecules, the two-exciton states are simply the three states corresponding to the symmetric overtone, the asymmetric overtone, and their combination band. The uncoupled DOS displayed on Fig. 10 has its maximum at 6705 cm⁻¹ and a full width half maximum (FWHM) of 790 cm⁻¹. We also show the harmonic DOS where the two-exciton states include states characterizing one exciton on one molecule and one exciton on another molecule. This has maximum at 6835 cm⁻¹ and FWHM of 580 cm⁻¹. The 130 cm⁻¹ shift between the two maxima is a signature of the intramolecular anharmonic couplings.

When the molecules are uncoupled, all states are localized. Two-exciton states made of excitons residing on two different molecules do not contribute to the signal. Consequently, the uncoupled \mathbf{k}_{III} signal can only show states ob-

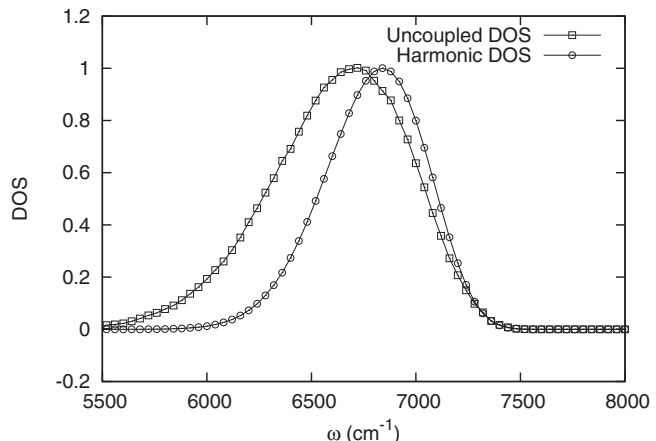


FIG. 10. Two-exciton DOS. Open square: uncoupled DOS. Open circle: harmonic DOS.

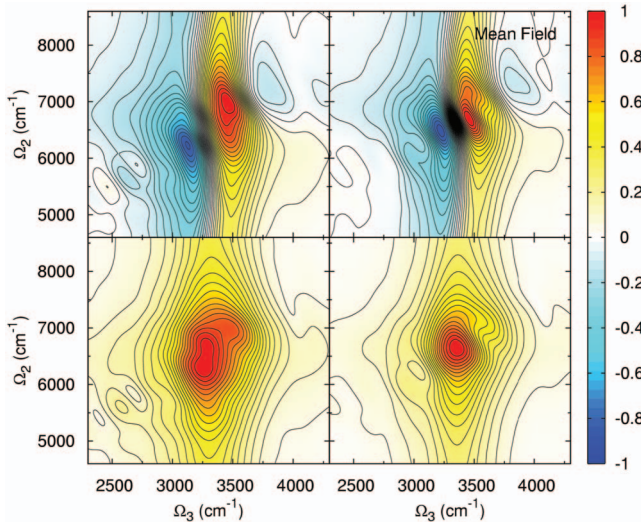


FIG. 11. (Color) k_{III} signal for $t_1=0$ with XXXX polarization: Full simulation (left column) and mean field approximation (right column). Upper row: imaginary part; lower row: absolute value. Each panel is normalized to its maximum.

served in the uncoupled DOS. In contrast when the molecules are coupled, these states which are not sensitive to the anharmonicity are observed. This explains the broader spectrum in the blue side for the coupled system.

In Fig. 9 we also compare the XXYY k_{III} signal for $t_1=0$ with the corresponding uncoupled signal. For uncoupled molecules, the XXXX and XXYY signals appear to be very similar in shape as we found in k_{I} . However, for coupled molecules, the two signals are very different.

Finally to explore the sensitivity of the double-quantum-coherence signal to the two-exciton coherence, we display in Fig. 11 the XXXX signal using the mean field approximation. The absolute value mean field signal is narrower, in particular, in the red tail. This is due to the absence of anharmonic shift in the two-exciton states.

V. CONCLUSIONS

In this paper, we have developed a new NEP algorithm for computing the coherent third order nonlinear signals of disordered excitons. This is based on a generalization of the NEE approach to include fluctuating Hamiltonian and transition dipoles. The various Liouville pathways are not calculated separately; the cancellation between them is built in from the outset. Our algorithm designed for large systems is

very efficient compared to similar methodologies. This formalism is used to compute the nonlinear signals k_{I} , k_{II} , and k_{III} for liquid water. The k_{I} signal is a powerful tool to observe the fast vibrational dynamics by varying the time t_2 . This dynamics is influenced by the frequency correlation, the transition dipole reorientation, and the excitonic coupling. However, for a fixed t_2 , it is insensitive to the intermolecular coupling and the two-exciton coherence. The same conclusion also applies to the k_{II} even though we found a slightly increased sensitivity in the intermolecular coupling. The double-quantum-coherence signals are complementary and appear to be very sensitive to both the couplings and the two-exciton coherence.

Recently observed $k_{\text{I}}+k_{\text{II}}$ signals^{3,30,31} in liquid water have shown a good correspondence with simulations for $t_2=0$ (see Ref. 3). However, a fast decay with delay time t_2 on a 100 fs time scale with a persistent GSB was observed. This relaxation was not included in our theoretical model. To reproduce both the decay and the persistent GSB, the simulation in Refs. 3 and 35 introduced an *ad hoc* population relaxation. A microscopic simulation of the population relaxation will be desirable. It is believed that the rapid population relaxation of the OH stretch is due to a Fermi resonance with the HOH bending.²⁹ Consequently, it will be necessary to include the bending mode explicitly in our simulations.

Due to its efficiency, this algorithm will be a great tool to predict nonlinear spectra. In particular, using the mean field approximation, it is now possible to compute the optical response of very large systems ($\sim 10^3$). This is of great interest, for example, to simulate water in biological environment.

ACKNOWLEDGMENTS

This work was supported by the National Institutes of Health Grant No. GM59230 and the National Science Foundation Grant No. CHE-0745891. The authors would like to thank A. Paarmann for providing the Hamiltonian trajectory and useful discussions. Many helpful discussions with Dr. Wei Zhuang and Dr. Darius Abramavicius are gratefully acknowledged.

APPENDIX A: RESPONSE FUNCTION FOR THE k_{II} TECHNIQUE

The $k_{\text{II}}=k_{\text{I}}-k_{\text{2}}+k_{\text{3}}$ signal is expressed as a sum of three terms,³⁶ in analogy with Eq. (6),

$$\begin{aligned} S_{\nu_4 \nu_3 \nu_2 \nu_1}^{k_{\text{II}}}(\tau_4, \tau_3, \tau_2, \tau_1) = & \left(\frac{i}{\hbar} \right)^3 \sum_{n_1 n_2 n_3 n_4} \mu_{n_1; \nu_1}(\tau_1) \mu_{n_2; \nu_2}(\tau_2) \mu_{n_3; \nu_3}(\tau_3) \mu_{n_4; \nu_4}(\tau_4) (\langle g | B_{n_4} \mathcal{U}(\tau_4, \tau_3) B_{n_3}^\dagger \mathcal{U}(\tau_3, \tau_2) B_{n_2} \mathcal{U}(\tau_2, \tau_1) B_{n_1}^\dagger | g \rangle \\ & + \langle g | B_{n_2} \mathcal{U}(\tau_2, \tau_3) B_{n_3}^\dagger \mathcal{U}(\tau_3, \tau_4) B_{n_4} \mathcal{U}(\tau_4, \tau_1) B_{n_1}^\dagger | g \rangle - \langle g | B_{n_4} \mathcal{U}(\tau_4, \tau_2) B_{n_2} \mathcal{U}(\tau_2, \tau_3) B_{n_3}^\dagger \mathcal{U}(\tau_3, \tau_1) B_{n_1}^\dagger | g \rangle). \quad (\text{A1}) \end{aligned}$$

Using Green's function [Eq. (9)] and the Bethe-Salpeter equation [Eq. (13)], we find the analog of Eq. (14),

$$\begin{aligned} S_{\nu_4 \nu_3 \nu_2 \nu_1}^{k_{II}}(\tau_4, \tau_3, \tau_2, \tau_1) &= 2 \left(\frac{i}{\hbar} \right)^4 \sum_{n_1 n_2 n_3 n_4} \sum_{m_1 m_2 m_3 m_4 p_1} \mu_{n_1; \nu_1}(\tau_1) \mu_{n_2; \nu_2}(\tau_2) \mu_{n_3; \nu_3}(\tau_3) \mu_{n_4; \nu_4}(\tau_4) \\ &\times \int_{\tau_3}^{\tau_4} ds G_{n_4, m_4}(\tau_4, s) U_{m_4 m_2 m_3 m_1}(s) \mathcal{G}_{m_3 m_1, n_3 p_1}(s, \tau_3) G_{p_1, n_1}(\tau_3, \tau_1) G_{m_2, n_2}^*(s, \tau_2). \end{aligned} \quad (\text{A2})$$

In terms of the wave function, the response function takes a similar form as for the k_1 technique [Eqs. (18) and (19)], except that the function $X_{m_4; \nu_3 \nu_2 \nu_1}$ [Eq. (20)] is

$$X_{m_4; \nu_3 \nu_2 \nu_1}^{k_{II}}(s; \tau_3, \tau_2, \tau_1) = \sum_{m_1 m_2 m_3} U_{m_4 m_2 m_3 m_1}(s) \psi_{m_3 m_1, \nu_3; \nu_1}^{(2)}(s; \tau_3; \tau_1) \psi_{m_2; \nu_2}^{(1)*}(s; \tau_2). \quad (\text{A3})$$

The Feynmann diagram corresponding to Eq. (A2) is displayed in Fig. 1(b).

APPENDIX B: RESPONSE FUNCTION FOR THE k_{III} TECHNIQUE

The $k_{III}=k_1+k_2-k_3$ signal is given by a sum of two terms³⁶ in analogy with Eq. (6),

$$\begin{aligned} S_{\nu_4 \nu_3 \nu_2 \nu_1}^{k_{III}}(\tau_4, \tau_3, \tau_2, \tau_1) &= \left(\frac{i}{\hbar} \right)^3 \sum_{n_1 n_2 n_3 n_4} \mu_{n_1; \nu_1}(\tau_1) \mu_{n_2; \nu_2}(\tau_2) \mu_{n_3; \nu_3}(\tau_3) \mu_{n_4; \nu_4}(\tau_4) \\ &\times \langle \langle g | B_{n_4} \mathcal{U}(\tau_4, \tau_3) B_{n_3} \mathcal{U}(\tau_3, \tau_2) B_{n_2}^\dagger \mathcal{U}(\tau_2, \tau_1) B_{n_1}^\dagger | g \rangle \rangle - \langle g | B_{n_3} \mathcal{U}(\tau_3, \tau_4) B_{n_4} \mathcal{U}(\tau_4, \tau_2) B_{n_2}^\dagger \mathcal{U}(\tau_2, \tau_1) B_{n_1}^\dagger | g \rangle \rangle. \end{aligned} \quad (\text{B1})$$

Using Green's function [Eq. (9)] and the Bethe-Salpeter equation [Eq. (13)], we find the analog of Eq. (14),

$$\begin{aligned} S_{\nu_4 \nu_3 \nu_2 \nu_1}^{k_{III}}(\tau_4, \tau_3, \tau_2, \tau_1) &= 2 \left(\frac{i}{\hbar} \right)^4 \sum_{n_1 n_2 n_3 n_4} \sum_{m_1 m_2 m_3 m_4 p_1} \mu_{n_1; \nu_1}(\tau_1) \mu_{n_2; \nu_2}(\tau_2) \mu_{n_3; \nu_3}(\tau_3) \mu_{n_4; \nu_4}(\tau_4) \\ &\times \int_{\tau_3}^{\tau_4} ds G_{n_4, m_4}(\tau_4, s) U_{m_4 m_3 m_2 m_1}(s) G_{m_3 m_1, n_3 p_1}^*(s, \tau_3) \mathcal{G}_{m_2 m_1, n_2 p_1}(s, \tau_2) G_{p_1, n_1}(\tau_2, \tau_1). \end{aligned} \quad (\text{B2})$$

In terms of the wave function, the response function takes a similar form as for the k_1 technique [Eqs. (18) and (19)], except that the function $X_{m_4; \nu_3 \nu_2 \nu_1}$ [Eq. (20)] is

$$\begin{aligned} X_{m_4; \nu_3 \nu_2 \nu_1}^{k_{III}}(s; \tau_3, \tau_2, \tau_1) &= \sum_{m_1 m_2 m_3} U_{m_4 m_3 m_2 m_1}(s) \\ &\times \psi_{m_2 m_1, \nu_2; \nu_1}^{(2)}(s; \tau_2; \tau_1) \psi_{m_3; \nu_3}^{(1)*}(s; \tau_3). \end{aligned} \quad (\text{B3})$$

The Feynmann diagram corresponding to Eq. (B1) is displayed in Fig. 1(c).

APPENDIX C: CALCULATING THE RESPONSE WITH THE NEEs

In Sec. II, the third order response function was derived starting with sum-over-states expressions [Eq. (6)]. Alternatively, the response function can be derived in the quasiparticle picture. The derivation starts by considering the expectation value of the polarization operator,

$$\hat{P}(\tau) = \sum_m \mu_m(\tau) (\hat{B}_m^\dagger(\tau) + \hat{B}_m(\tau)), \quad (\text{C1})$$

which is obtained from the Heisenberg equation of motion for operators,

$$i\hbar \frac{\partial}{\partial \tau} \hat{B}_k = [\hat{B}_k, \hat{H}(\tau)], \quad (\text{C2})$$

followed by a trace over the initial density matrix ($|g\rangle\langle g|$),

$$\begin{aligned} i\hbar \frac{\partial \langle \hat{B}_k \rangle}{\partial \tau} &= \sum_n h_{kn}(\tau) \langle \hat{B}_n \rangle + 2 \sum_{m, m', n'} U_{knm' n'}(\tau) \langle \hat{B}_n^\dagger \hat{B}_{m'} \hat{B}_{n'} \rangle \\ &- \boldsymbol{\mu}_k(\tau) \cdot \mathbf{E}(\tau). \end{aligned} \quad (\text{C3})$$

This equation is not closed since it depends on $\langle \hat{B}_n^\dagger \hat{B}_{m'} \hat{B}_{n'} \rangle$. As described in Ref. 9, this leads to an infinite hierarchy of many-body equations of motion to be solved simultaneously. These equations can be closed by assuming various types of factorization schemes and by neglecting terms above fourth order in the fields.¹ Here, we adopt the coherent limit factorization, $\langle \hat{B}_n^\dagger \hat{B}_{m'} \hat{B}_{n'} \rangle = \langle \hat{B}_n^\dagger \rangle \langle \hat{B}_{m'} \hat{B}_{n'} \rangle$. The range of validity of this approximation is discussed in Ref. 2. In this case, the polarization is obtained by solving the following set of equations:

$$\begin{aligned} i\hbar \frac{\partial B_k}{\partial \tau} &= \sum_n h_{kn}(\tau) B_n + 2 \sum_{n, m', n'} U_{knm' n'}(\tau) B_n^* Y_{m' n'} \\ &- \lambda \boldsymbol{\mu}_k(\tau) \cdot \mathbf{E}(\tau), \end{aligned} \quad (\text{C4})$$

$$i\hbar \frac{\partial Y_{kl}}{\partial \tau} = \sum_{mn} (h_{kl,mn}^{(y)}(\tau) + 2U_{klmn}(\tau))Y_{mn} - \lambda \boldsymbol{\mu}_k(\tau) \cdot \mathbf{E}(\tau)B_l - \lambda \boldsymbol{\mu}_l(\tau) \cdot \mathbf{E}(\tau)B_k, \quad (\text{C5})$$

where $B_k = \langle \hat{B}_k \rangle$, $Y_{kl} = \langle \hat{B}_k \hat{B}_l \rangle$ and where $h_{kl,mn}^{(y)}(\tau) = \delta_{km}h_{ln}(\tau) + \delta_{ln}h_{km}(\tau)$.

The parameter λ keeps track of the powers in the external fields (λ will be set to 1 in the end). We seek a solution for $B_k(\tau)$ in powers of the external fields,

$$B_k(\tau) = B_k^{(0)}(\tau) + \lambda B_k^{(1)}(\tau) + \lambda^2 B_k^{(2)}(\tau) + \lambda^3 B_k^{(3)}(\tau) + \dots, \quad (\text{C6})$$

$$Y_{kl}(\tau) = Y_{kl}^{(0)}(\tau) + \lambda Y_{kl}^{(1)}(\tau) + \lambda^2 Y_{kl}^{(2)}(\tau) + \lambda^3 Y_{kl}^{(3)}(\tau) + \dots \quad (\text{C7})$$

These are then inserted into Eqs. (C4) and (C5) and solved order by order in λ . It is easy to show that $B_k^{(0)}(\tau)=0$ and $Y_{kl}^{(0)}(\tau)=0$ for our initial equilibrium density matrix where the system is in the ground state. The first nonzero contribution is of order of 1 in λ ,

$$i\hbar \frac{\partial B_k^{(1)}}{\partial \tau} = \sum_n h_{kn}(\tau)B_n^{(1)} - \boldsymbol{\mu}_k(\tau) \cdot \mathbf{E}(\tau), \quad (\text{C8})$$

$$i\hbar \frac{\partial Y_{kl}^{(1)}}{\partial \tau} = \sum_{mn} (h_{kl,mn}^{(y)}(\tau) + 2U_{klmn}(\tau))Y_{mn}^{(1)}. \quad (\text{C9})$$

To this order, the equations for B and Y are independent, their solutions are

$$B_k^{(1)}(\tau) = \frac{i}{\hbar} \sum_n \int_0^\tau d\tau' G_{kn}(\tau, \tau') \boldsymbol{\mu}_n(\tau') \cdot \mathbf{E}(\tau'), \quad (\text{C10})$$

$$Y_{kl}^{(1)}(\tau) = 0, \quad (\text{C11})$$

where the single exciton Green's function G is defined by Eq. (8). To second order in λ , we get

$$i\hbar \frac{\partial B_k^{(2)}}{\partial \tau} = \sum_n h_{kn}(\tau)B_n^{(2)}, \quad (\text{C12})$$

$$i\hbar \frac{\partial Y_{kl}^{(2)}}{\partial \tau} = \sum_{mn} (h_{kl,mn}^{(y)}(\tau) + 2U_{klmn}(\tau))Y_{mn}^{(2)} - \boldsymbol{\mu}_k(\tau) \cdot \mathbf{E}(\tau)B_l^{(1)} - \boldsymbol{\mu}_l(\tau) \cdot \mathbf{E}(\tau)B_k^{(1)}, \quad (\text{C13})$$

which give the following solutions:

$$B_k^{(2)}(\tau) = 0, \quad (\text{C14})$$

$$Y_{kl}^{(2)}(\tau) = \frac{i}{\hbar} \sum_{mn} \int_0^\tau d\tau' G_{kl,mn}(\tau, \tau') \boldsymbol{\mu}_m(\tau) \cdot \mathbf{E}(\tau') B_n^{(1)}(\tau'), \quad (\text{C15})$$

where the double exciton Green's function G is defined by Eq. (9). Note that $B_k^{(2)}(\tau)=0$ implies that the second order response function vanishes.

The third order equations of motion for B are

$$i\hbar \frac{\partial B_k^{(3)}}{\partial \tau} = \sum_n h_{kn}(\tau)B_n^{(3)} + 2 \sum_{m_3, m_2, m_1} U_{k, m_3, m_2, m_1}(\tau) B_{m_1}^{(1)*} Y_{m_3 m_2}^{(2)}, \quad (\text{C16})$$

whose solution does not require the knowledge of $Y_{mn}^{(3)}$. Hence, Green's function solution for $B_k^{(3)}$ is

$$B_k^{(3)}(\tau) = -\frac{2i}{\hbar} \sum_{m_4, m_3, m_2, m_1} \int_0^\tau ds G_{km_4}(\tau, s) \times U_{m_4 m_1, m_3 m_2}(s) B_{m_1}^{(1)*}(s) Y_{m_3 m_2}^{(2)}(s). \quad (\text{C17})$$

Using Eqs. (C10) and (C15), we obtain the following expressions for $B_k^{(3)}(\tau)$:

$$B_k^{(3)}(\tau) = 2 \left(\frac{i}{\hbar} \right)^4 \sum_{m_1, m_2, m_3, m_4} \sum_{n_1, n_2, n_3, p_2} \times \int_0^\tau ds \int_0^s d\tau_1 \int_0^s d\tau_3 \int_0^{\tau_3} d\tau_2 \times G_{km_4}(\tau, s) U_{m_4 m_1 m_3 m_2}(s) G_{m_1 n_1}^*(s, \tau_1) \mathcal{G}_{m_3 m_2, n_3 p_2}(s, \tau_3) G_{p_2, n_2}(\tau_3, \tau_2) \times (\boldsymbol{\mu}_{n_1}(\tau_1) \cdot \mathbf{E}(\tau_1)) (\boldsymbol{\mu}_{n_2}(\tau_2) \cdot \mathbf{E}(\tau_2)) (\boldsymbol{\mu}_{n_3}(\tau_3) \cdot \mathbf{E}(\tau_3)). \quad (\text{C18})$$

The third order polarization is given by $P^{(3)}(\tau_4) = \sum_{n_4} \boldsymbol{\mu}_{n_4}(\tau_4) (B_{n_4}^{(3)}(\tau_4) + (B_{n_4}^{(3)}(\tau_4))^*)$. This contains all contributions to the third order signal (\mathbf{k}_I , \mathbf{k}_{II} , and \mathbf{k}_{III}). The polarization that will induce a signal in the \mathbf{k}_I direction is given by

$$\mathbf{P}_{\mathbf{k}_I}^{(3)}(\tau_4) = 2 \left(\frac{i}{\hbar} \right)^4 \sum_{n_1, n_2, n_3, n_4} \sum_{m_1, m_2, m_3, m_4, p_2} \boldsymbol{\mu}_{n_4}(\tau_4) \times \int_0^{\tau_4} ds \int_0^s d\tau_3 \int_0^{\tau_3} d\tau_2 \int_0^{\tau_2} d\tau_1 \times G_{n_4 m_4}(\tau_4, s) U_{m_4 m_1, m_3 m_2}(s) G_{m_3 m_2, n_3 p_2}(s, \tau_3) G_{p_2, n_2}(\tau_3, \tau_2) G_{m_1 n_1}^*(s, \tau_1) \times (\boldsymbol{\mu}_{n_1}(\tau_1) \cdot \mathbf{E}(\tau_1)) (\boldsymbol{\mu}_{n_2}(\tau_2) \cdot \mathbf{E}(\tau_2)) (\boldsymbol{\mu}_{n_3}(\tau_3) \cdot \mathbf{E}(\tau_3)), \quad (\text{C19})$$

where $\tau_1 < \tau_2 < \tau_3$ are the respective time of action of the three pulses. From the relation

$$\begin{aligned} P_{k_1, \nu_4}^{(3)}(\tau_4) = & \int_0^{\tau_4} d\tau_3 \int_0^{\tau_3} d\tau_2 \int_0^{\tau_2} d\tau_1 \\ & \times S_{\nu_4 \nu_3 \nu_2 \nu_1}^{k_1}(\tau_4, \tau_3, \tau_2, \tau_1) E_{\nu_3}(\tau_3) E_{\nu_2}(\tau_2) E_{\nu_1}(\tau_1), \end{aligned} \quad (\text{C20})$$

we recover the expression of the k_1 response function, Eq. (14), which was obtain in the sum-over-states representation.

APPENDIX D: THE NUMERICAL INTEGRATION PROCEDURE

1. Wave function propagation

Our vibrational system has three characteristic energy scales: The vibrational frequency ω_0 , the dephasing Γ , and the exciton coupling J . The vibrational frequency of the OH stretch of water $\omega_0 \sim 3400 \text{ cm}^{-1}$. Γ originates from fast frequency fluctuations. In general, the bath has multiple time scales. In vibrational spectroscopy, the shortest time is typically around 50 fs (corresponding to hydrogen bonding dynamics). This gives $\Gamma \sim 100 \text{ cm}^{-1}$. J represents the exciton coupling between the optically active vibrational modes, off-diagonal elements of h_{ij} . The coupling between the two OH stretching modes in a water is $J \sim 30 \text{ cm}^{-1}$.⁴³ (For the amide-I vibrations in peptide we have $\omega_0 \sim 1650 \text{ cm}^{-1}$ and $J \sim 10 \text{ cm}^{-1}$.)

By taking the time step $\Delta\tau$ to be small compared to the bath dephasing $\Delta\tau \ll 1/\Gamma$, we can assume that the Hamiltonian is constant over this period of time. For each t such as $\tau \leq t < \tau + \Delta\tau$, we have $H(t) = H(\tau)$, the Schrödinger equation for the one-exciton wave function can then be solved during this interval,

$$|\psi_{\nu_1}^{(1)}(\tau + \Delta\tau; \tau_1)\rangle \approx \exp\left[-\frac{i}{\hbar}H(\tau)\Delta\tau\right]|\psi_{\nu_1}^{(1)}(\tau; \tau_1)\rangle. \quad (\text{D1})$$

To calculate this exponential, the Hamiltonian is divided into a local and a nonlocal part. $H = H_0 + \Delta H$. To simplify the

notation, the τ dependence of the Hamiltonian is not written explicitly. The local part corresponds to the local frequencies,

$$H_0 = \sum_i h_{ii} B_i^\dagger B_i + \sum_{ij} U_{ijij} B_i^\dagger B_j^\dagger B_j B_i, \quad (\text{D2})$$

while the nonlocal part corresponds to the exciton coupling $\Delta H = H - H_0$. Typically for the one-exciton states $H_0 \sim \omega_0$ and $\Delta H \sim J$. The one-exciton wave function is

$$\begin{aligned} |\psi_{\nu_1}^{(1)}(\tau + \Delta\tau; \tau_1)\rangle & \approx e^{-iH_0\Delta\tau/\hbar} \\ & \times \exp_+ \left[-\frac{i}{\hbar} \int_0^{\Delta\tau} dt e^{iH_0 t/\hbar} \Delta H e^{-iH_0 t/\hbar} \right] \\ & \times |\psi_{\nu_1}^{(1)}(\tau; \tau_1)\rangle. \end{aligned} \quad (\text{D3})$$

Expanding Green's function up to the order ΔH^2 and using a trapezoidal rule⁴⁴ to numerically evaluate the integrals, we find

$$\begin{aligned} |\psi_{\nu_1}^{(1)}(\tau + \Delta\tau; \tau_1)\rangle & \approx \left\{ e^{-iH_0\Delta\tau/\hbar} - i\frac{\Delta\tau}{2} \left(1 - i\frac{\Delta\tau}{2} \Delta H \right) \right. \\ & \times \left. [e^{-iH_0\Delta\tau/\hbar} \Delta H + \Delta H e^{-iH_0\Delta\tau/\hbar}] \right\} \\ & \times |\psi_{\nu_1}^{(1)}(\tau; \tau_1)\rangle. \end{aligned} \quad (\text{D4})$$

In a similar fashion, we can obtain the propagation of the two-exciton wave function,

$$\begin{aligned} |\psi_{\nu_1 \nu_2}^{(2)}(\tau + \Delta\tau; \tau_2; \tau_1)\rangle & \approx \left\{ e^{-iH_0\Delta\tau/\hbar} - i\frac{\Delta\tau}{2} \left(1 - i\frac{\Delta\tau}{2} \Delta H \right) \right. \\ & \times \left. [e^{-iH_0\Delta\tau/\hbar} \Delta H + \Delta H e^{-iH_0\Delta\tau/\hbar}] \right\} \\ & \times |\psi_{\nu_1 \nu_2}^{(2)}(\tau; \tau_2; \tau_1)\rangle. \end{aligned} \quad (\text{D5})$$

2. Response function propagation

The response function is expressed in terms of the vector $R_{n_4; \nu_3 \nu_2 \nu_1}^{k_1}$ [Eq. (19)]. At time $\tau + \Delta\tau$ we have

$$\begin{aligned} R_{n_4; \nu_3 \nu_2 \nu_1}^{k_1}(\tau_4 + \Delta\tau, \tau_3, \tau_2, \tau_1) & = \sum_{m_4} G_{n_4, m_4}(\tau_4 + \Delta\tau, \Delta\tau) R_{m_4; \nu_3 \nu_2 \nu_1}^{k_1}(\tau_4, \tau_3, \tau_2, \tau_1) \\ & + \sum_{m_4} \int_{\tau_4}^{\tau_4 + \Delta\tau} ds G_{n_4, m_4}(\tau_4 + \Delta\tau, s) X_{m_4; \nu_3 \nu_2 \nu_1}^{k_1}(s; \tau_3, \tau_2, \tau_1). \end{aligned} \quad (\text{D6})$$

The trapezoidal rule gives

$$\begin{aligned} R_{n_4; \nu_3 \nu_2 \nu_1}^{k_1}(\tau_4 + \Delta\tau, \tau_3, \tau_2, \tau_1) & \approx \sum_{m_4} G_{n_4, m_4}(\tau_4 + \Delta\tau, \Delta\tau) R_{m_4; \nu_3 \nu_2 \nu_1}^{k_1}(\tau_4, \tau_3, \tau_2, \tau_1) \\ & + \frac{\Delta\tau}{2} \left[X_{n_4; \nu_3 \nu_2 \nu_1}^{k_1}(\tau + \Delta\tau; \tau_3, \tau_2, \tau_1) + \sum_{m_4} G_{n_4, m_4}(\tau + \Delta\tau, s) X_{m_4; \nu_3 \nu_2 \nu_1}^{k_1}(\tau; \tau_3, \tau_2, \tau_1) \right]. \end{aligned} \quad (\text{D7})$$

In Eq. (D7), Green's function is not directly computed. Instead, the function $R_{m;\nu_3\nu_2\nu_1}^{k_1}(\tau_4+\Delta\tau, \tau_3, \tau_2, \tau_1)$ is propagated in a similar fashion as for the one-exciton wave function [see Eq. (D4)].

- ¹S. Mukamel, *Principles of Nonlinear Optical Spectroscopy* (Oxford University Press, New York, 1995).
- ²D. Abramavicius, B. Palmieri, L. Yang, D. Voronine, and S. Mukamel, *Chem. Rev.* (Washington, D.C.) (in press).
- ³A. Paarmann, T. Hayashi, S. Mukamel, and R. J. D. Miller, *J. Chem. Phys.* **128**, 191103 (2008).
- ⁴Y. L. Li, L. Huang, R. J. D. Miller, T. Hasegawa, and Y. Tanimura, *J. Chem. Phys.* **128**, 234507 (2008).
- ⁵W. Zhuang, T. Hayashi, and S. Mukamel, *Angew. Chem.* (in press).
- ⁶F. C. Spano and S. Mukamel, *Phys. Rev. A* **41**, 5243 (1990).
- ⁷F. C. Spano and S. Mukamel, *Phys. Rev. Lett.* **66**, 1197 (1991).
- ⁸F. C. Spano and S. Mukamel, *J. Chem. Phys.* **95**, 7526 (1991).
- ⁹V. Chernyak, W. M. Zhang, and S. Mukamel, *J. Chem. Phys.* **109**, 9587 (1998).
- ¹⁰W. M. Zhang, V. Chernyak, and S. Mukamel, *J. Chem. Phys.* **110**, 5011 (1999).
- ¹¹S. Mukamel, *Annu. Rev. Phys. Chem.* **51**, 691 (2000).
- ¹²T. L. C. Jansen, W. Zhuang, and S. Mukamel, *J. Chem. Phys.* **121**, 10577 (2004).
- ¹³T. L. C. Jansen and J. Knoester, *J. Phys. Chem. B* **110**, 22910 (2006).
- ¹⁴H. Torii, *J. Phys. Chem. A* **110**, 4822 (2006).
- ¹⁵R. Bloem, A. G. Dijkstra, T. L. C. Jansen, and J. Knoester, *J. Chem. Phys.* **129**, 055101 (2008).
- ¹⁶T. L. C. Jansen and J. Knoester, *Biophys. J.* **94**, 1818 (2008).
- ¹⁷B. M. Auer and J. L. Skinner, *J. Chem. Phys.* **127**, 104105 (2007).
- ¹⁸T. L. C. Jansen and W. M. Ruszel, *J. Chem. Phys.* **128**, 214501 (2008).
- ¹⁹S. Mukamel, R. Oszwaldowski, and D. Abramavicius, *Phys. Rev. B* **75**, 245305 (2007).
- ²⁰R. Laenen, K. Simeonidis, and A. Laubereau, *J. Phys. Chem. B* **106**, 408 (2002).
- ²¹S. Woutersen, U. Emmerichs, H.-K. Nienhuys, and H. J. Bakker, *Phys. Rev. Lett.* **81**, 1106 (1998).
- ²²H. J. Bakker, Y. L. A. Rezus, and R. L. A. Timmer, *J. Phys. Chem. A* **112**, 11523 (2008).
- ²³C. J. Fecko, J. D. Eaves, J. J. Loparo, A. Tokmakoff, and P. L. Geissler, *Science* **301**, 1698 (2003).
- ²⁴J. Stenger, D. Madsen, P. Hamm, E. T. J. Nibbering, and T. Elsaesser, *Phys. Rev. Lett.* **87**, 027401 (2001).
- ²⁵A. M. Dokter, S. Woutersen, and H. J. Bakker, *Proc. Natl. Acad. Sci. U.S.A.* **103**, 15355 (2006).
- ²⁶I. R. Piletic, H.-S. Tan, and M. D. Fayer, *J. Phys. Chem. B* **109**, 21273 (2005).
- ²⁷I. R. Piletic, D. E. Moilanen, D. B. Spry, N. E. Levinger, and M. D. Fayer, *J. Phys. Chem. A* **110**, 4985 (2006).
- ²⁸S. Park, D. E. Moilanen, and M. D. Fayer, *J. Phys. Chem. B* **112**, 5279 (2008).
- ²⁹A. J. Lock and H. J. Bakker, *J. Chem. Phys.* **117**, 1708 (2002).
- ³⁰M. L. Cowan, B. D. Bruner, N. Huse, J. R. Dwyer, B. Chugh, E. T. J. Nibbering, T. Elsaesser, and R. J. D. Miller, *Nature (London)* **434**, 199 (2005).
- ³¹D. Kraemer, M. L. Cowan, A. Paarmann, N. Huse, E. T. J. Nibbering, T. Elsaesser, and R. J. D. Miller, *Proc. Natl. Acad. Sci. U.S.A.* **105**, 437 (2008).
- ³²D. Cringus, J. Lindner, M. T. W. Milder, M. S. Pshenichnikov, P. Vöhringer, and D. A. Wiersma, *Chem. Phys. Lett.* **408**, 162 (2005).
- ³³K. Lazonder, M. S. Pshenichnikov, and D. A. Wiersma, *Opt. Lett.* **31**, 3354 (2006).
- ³⁴D. Cringus, A. Bakulin, J. Lindner, P. Vöhringer, M. S. Pshenichnikov, and D. A. Wiersma, *J. Phys. Chem. B* **111**, 14193 (2007).
- ³⁵A. Paarmann, T. Hayashi, S. Mukamel, and R. J. D. Miller (unpublished).
- ³⁶S. Mukamel and D. Abramavicius, *Chem. Rev. (Washington, D.C.)* **104**, 2073 (2004).
- ³⁷J. A. Leegwater and S. Mukamel, *Phys. Rev. A* **46**, 452 (1992).
- ³⁸T. L. C. Jansen, T. Hayashi, W. Zhuang, and S. Mukamel, *J. Chem. Phys.* **123**, 114504 (2005).
- ³⁹K. Kwak, D. E. Rosenfeld, and M. D. Fayer, *J. Chem. Phys.* **128**, 204505 (2008).
- ⁴⁰S. Woutersen and H. J. Bakker, *Nature (London)* **402**, 507 (1999).
- ⁴¹H. Torii, *J. Phys. Chem. A* **110**, 9469 (2006).
- ⁴²S. Mukamel, R. Oszwaldowski, and L. Yang, *J. Chem. Phys.* **127**, 221105 (2007).
- ⁴³B. M. Auer and J. L. Skinner, *J. Chem. Phys.* **128**, 224511 (2008).
- ⁴⁴W. H. Press, S. A. Teukolsky, W. T. Vetterling, and B. P. Flannery, *Numerical Recipes*, 3rd ed. (Cambridge University Press, Cambridge, 2007).